Supporting Information

Unprecedented direct spatiotemporal imaging of a reversible interface propagation in a switchable cooperative Fe(III) spin crossover material

Marcos A. Bento,[a] Nour el islam Belmouri,[b] André Fernandes,[a] David Ndrio,[c] Guillaume Bouchez,[b] Longhe Li,[b] Liliana P. Ferreira,[d,e] Hermínio P. Diogo,[f] João Rocha,[g] Francesc Viñes,[c] Adrià Gil,[h] Kamel Boukheddaden*,[b] Paulo N. Martinho*[a]

[a] *Centro de Química Estrutural, Institute of Molecular Sciences, Departamento de Química e Bioquímica, Faculdade de Ciências, Universidade de Lisboa, Campo Grande, 1749-016 Lisboa, Portugal*

[b] *Groupe d'Etudes de la Matière Condensée, CNRS UMR 8635, Université Paris Saclay-Versailles, 45 Avenue des Etats Unis 78035, Versailles, France.*

[c] *Departament de Ciència de Materials i Química Física & Institut de Química Teòrica i Computacional (IQTCUB), Universitat de Barcelona, c/ Martí i, Franquès 1–11, 08028 Barcelona, Spain*

[d] *Department of Physics, University of Coimbra, 3004-516 Coimbra, Portugal*

[e] *Centro de Física Teórica e Computacional, Faculdade de Ciências, Universidade de Lisboa, Portugal*

[f] *Centro de Química Estrutural, Institute of Molecular Sciences, Instituto Superior Técnico, Universidade de Lisboa, Portugal*

[g] *Department of Chemistry, CICECO-Aveiro Institute of Materials, University of Aveiro, Portugal*

[h] *Departament de Química, Física i Ciències Ambientals i del Sòl, ETSEA – Escola Tècnica Superior d'Enginyeria Agrària, Universitat de Lleida, Av. de l'alcalde Rovira Roure, 191, E25198, Lleida, Catalunya, Spain*

1. Synthesis and Structural Characterisation

Materials and methods: *N*-Ethylethylenediamine (98 %), 3-Ethoxysalicylaldehyde (97 %), Fe(III) nitrate (97 %), and solvents were used without further purification and purchased from merck, abcr, chemlab and honeywell. FTIR spectra were obtained on a Buker Invenio-S fourier transform infrared spectrometer in the 400-4000 cm^{-1} range with 4 cm^{-1} resolution using KBr pellets. Elemental analysis (EA) for C, H and N were performed with a Truspec Micro CHNS 630 200 200 elemental analyzer at the Department of Chemistry, University of Aveiro. Analysis parameters: sample amount 1.3 - 2.0 mg; combustion furnace temperature 1075 ºC; afterburner temperature 850 ºC. Detection method: C, H and S through infrared absorption; N by thermal conductivity. Gases required: combustion - oxygen; carrier helium; pneumatic - compressed air.

Synthesis of $[Fe(3\text{-}EtO\text{-}salEen)_2]NO_3$ (1): 3-Ethoxysalicylaldehyde (332 mg, 2 mmol) was added to a solution of *N*-Ethylethylenediamine (210 µL, 2 mmol) in methanol (20 mL) and left under stirring for 15 min to yield a light-yellow solution. Iron(III) nitrate (404 mg, 1 mmol) was added to the previous reaction mixture and left under stirring for 1:30 h. The solution immediately turned dark blue. Afterwards, the solution was filtered, and a dark blue precipitate was obtained. The deep dark blue solid obtained was recrystallized by slow evaporation in an acetonitrile solution and dark crystals were obtained (143 mg, 0.24 mmol) with a yield of 24 %. IR (KBr): $\tilde{\nu}_{max}/cm^{-1}$: 3173 ($\tilde{\nu}$NH, m), 2986-2871 ($\tilde{\nu}$CH, m), 1626 ($\tilde{\nu}$C=N, s), 1597 ($\tilde{\nu}$C=C, w), 1385 ($\tilde{\nu}NO_3$, s). Elemental Anal. Calcd (%) for $C_{26}H_{38}FeN_5O_7$: C, 53.07; H, 6.51; N, 11.90. Found: C, 52.84; H, 6.45; N, 11.77%.

Physical Measurements: Magnetisation measurements as a function of temperature were performed using a SQUID magnetometer (Quantum Design MPMS). The curves were obtained at 1000 Oe for temperatures ranging between 10 and 370 K. Several sequences of cooling and heating were performed using a scan rate of 5 K min^{-1} and measurements were taken in steps of 5 K. *Settle mode* was used for all temperatures stabilisation. The collected data were corrected for diamagnetic contributions.

Calorimetric measurements were performed using a 2920 MDSC system (TA Instruments Inc.) operated in conventional DSC mode. Samples with masses typically ranging from 2 to 5 mg were sealed in aluminum pans and weighed with a precision of $\pm 1.0 \times 10^{-4}$ mg using a Mettler UMT2 ultra-microbalance. The analyses were carried out at scanning rates of 2.5 and 5.0 $K \cdot min^{-1}$. Helium (Air Liquide N55) was used as the purge gas at a flow rate of 30 $cm^3 \cdot min^{-1}$. The baseline was corrected by recording a scan over the same temperature range using an empty reference pan. The temperature scale of the instrument was calibrated at the same heating rates using the fusion temperatures of *n*-decane (T_{fus} = 243.75 K), *n*-octadecane (T_{fus} = 301.77 K), hexatriacontane (T_{fus} = 347.30 K), indium (T_{fus} = 429.75 K), and tin (T_{fus} = 506.03 K), considering the onset temperatures. The organic standards were high-purity products from Fluka, while the metallic standards were supplied by TA Instruments. The heat-flow scale was calibrated using indium ($\Delta h_{(}$fus$_{)}$ = 28.71 $J \cdot g^{-1}$). Data analysis was performed using the TA Universal Analysis 2000 software (version 4.0).

Single crystal X-ray diffraction data of complex **1** was collected at 150 and at 353 K on a RIGAKU XtaLAB Synergy-i equipped with a Mo Kα (λ = 0.71073 Å) PhotonJet-i microsource, a HyPix3000 detector controlled by the CrysAlisPro software (Y. Oxford Diffraction Ltd, England, 2022, CrysAlis PRO, Rigaku V1.171.142.173a) and equipped with an Oxford Cryosystems Series 800 cryostream. Diffraction images were processed using the CrysAlisPro software and data was corrected for absorption by the multi-scan absorption correction using spherical harmonics implemented in SCALE3 ABSPACK scaling algorithm. The structures were solved by the direct methods using SHELXT 2014/5 and refined by weighted full matrix least-squares method on F2 using SHELXL2018/3.[72,81] All non-hydrogen atoms were refined with anisotropic thermal parameters. Molecular diagrams were drawn with Mercury software.[81] The Crystal data and selected refinement details at 353 K are listed in Supplementary Table 1.

Powder X-ray Diffraction diffractograms were obtained using a Philips Analytical PW 3050/60 X'Pert PRO automatic diffractometer, equipped with an X'Celerator detector. Data was acquired using X'Pert Data Collector version 2.0b software. CuKα was used as the radiation source, operating with a current of 30 mA and a voltage of 40 kV using a continuous scan of the Bragg angles (2θ) between 5º and 50º, with a step of 0.017 and an acquisition time of 200 s per step.

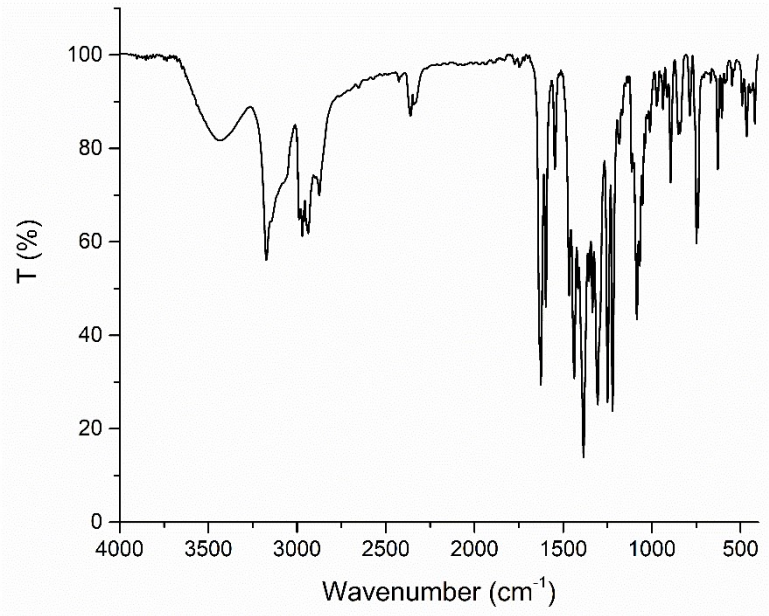

Supplementary Figure 1: FTIR spectrum of **1** in KBr pellets.

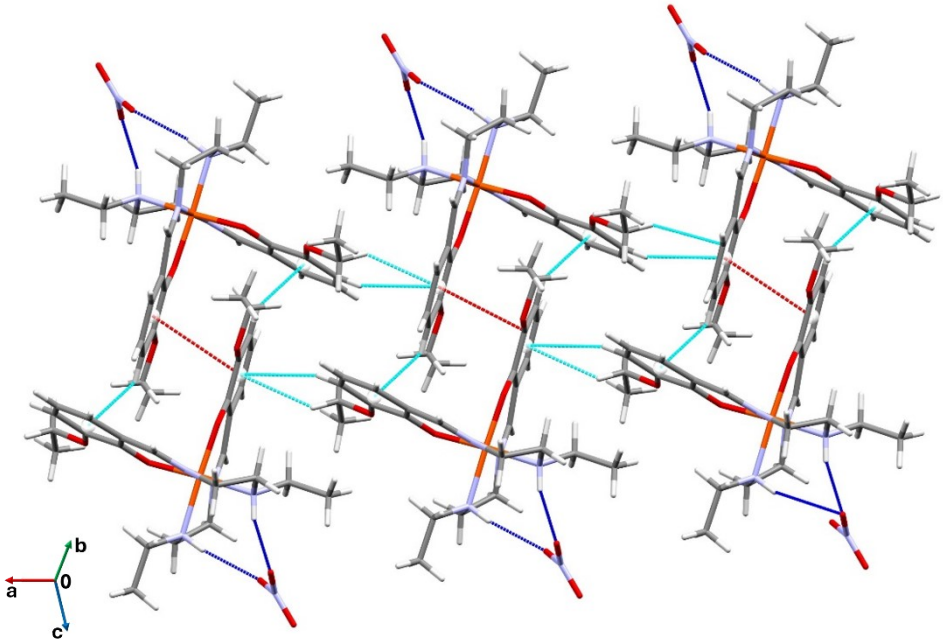

Supplementary Figure 2: Interactions between neighboring molecules of **1** at 150 K by the parallel fourfold aryl embrace (P4AE), C–H···π interactions (light blue), π···π (red), and N–H···O interactions (dark blue).

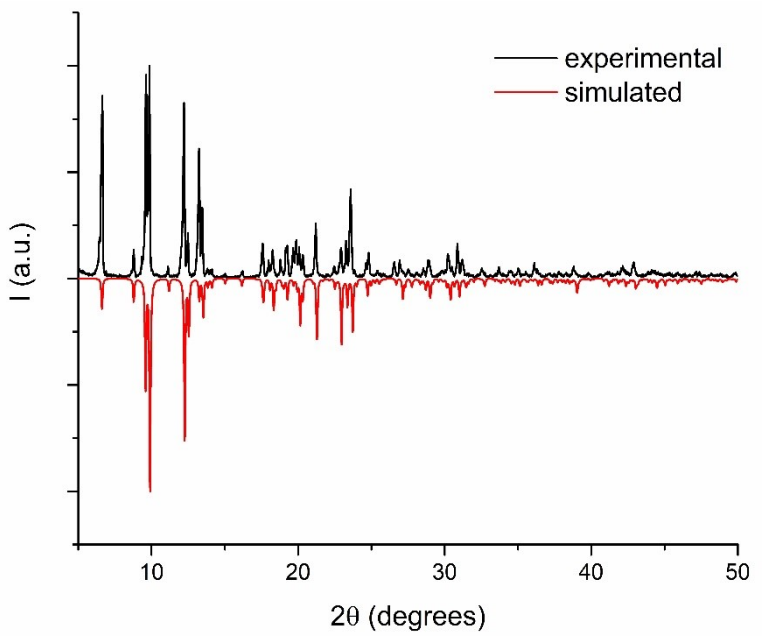

Supplementary Figure 3: Phase purity of a bulk sample of **1** determined by powder X-ray diffraction at 295 K (LS) and comparison with the simulated pattern generated by single crystal XRD.

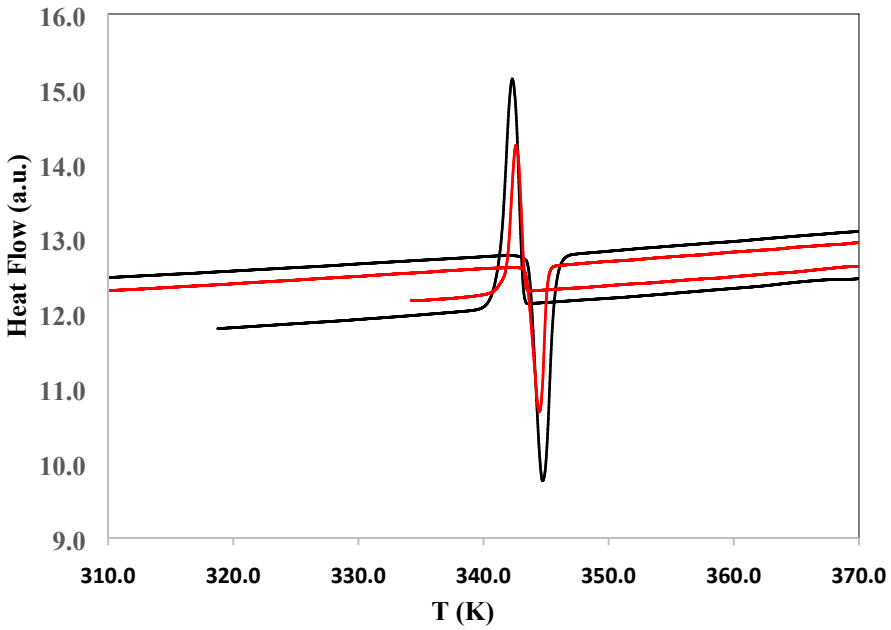

Supplementary Figure 4: DSC for **1** at a scan rate of 5 K·min^{-1} (black) and 2.5 K·min^{-1} (red).

Supplementary Table 1. Crystal data and refinement parameters of **1**.

Temperature (K)	**150**	**353**
Empirical Formula	$C_{26}H_{38}FeN_5O_7$	$C_{26}H_{38}FeN_5O_7$
M_w	588.46	588.46
aCrystal system	Triclinic	Triclinic
Space group	*Pī*	*Pī*
a / [Å]	9.6455(2)	10.0291(2)
b / [Å]	10.6472(2)	11.1775(4)
c / [Å]	14.2718(2)	13.9895(5)
α / [º]	100.2030(10)	93.434(3)
β / [º]	105.2210(10)	105.628(3)
γ / [º]	102.9980(10)	107.053(3)
V [Å^3]	1333.84	1776.38(4)
Z	2	2
D_c [Mg m^{-3}]	1.465	1.369
μ / [mm^{-1}]	0.620	0.580
F(000)	622	622
Crystal size [mm^3]	0.20 x 0.18 x 0.04	0.20 x 0.18 x 0.04
θ range for data collection (°)	2.028-28.094	1.928-28.145
Index ranges	-12≤*h*≤12, -14≤*k*≤14, -18≤l≤18	-12≤*h*≤13, -14≤*k*≤14, -18≤l≤17
Reflections collected	34836	44393
Unique reflections, [R_{int}]	6206[0.0470]	6633[0.0619]
Final *R* indices		
R_1, wR_2 [I>2σI]	0.0316, 0.0863 [5343]	0.0524, 0.1389 [4508]
Data/restraints/ parameters	6206/0/364	6633/0/356
Goodness-of-fit on F^2	1.038	1.066

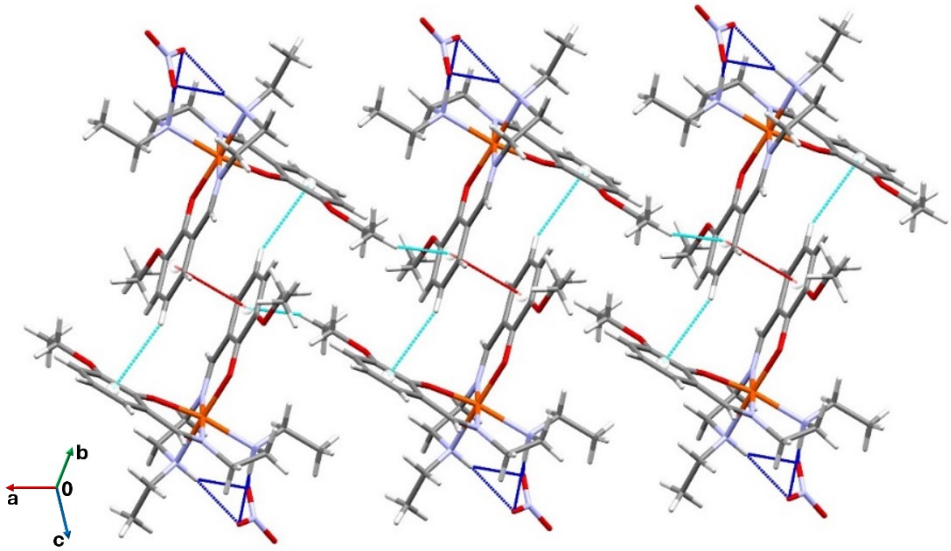

Supplementary Figure 5: Interactions between neighboring molecules of **1** at 353 K by the parallel fourfold aryl embrace (P4AE), C–H···π interactions (light blue), π···π (red), and N–H···O interactions (dark blue).

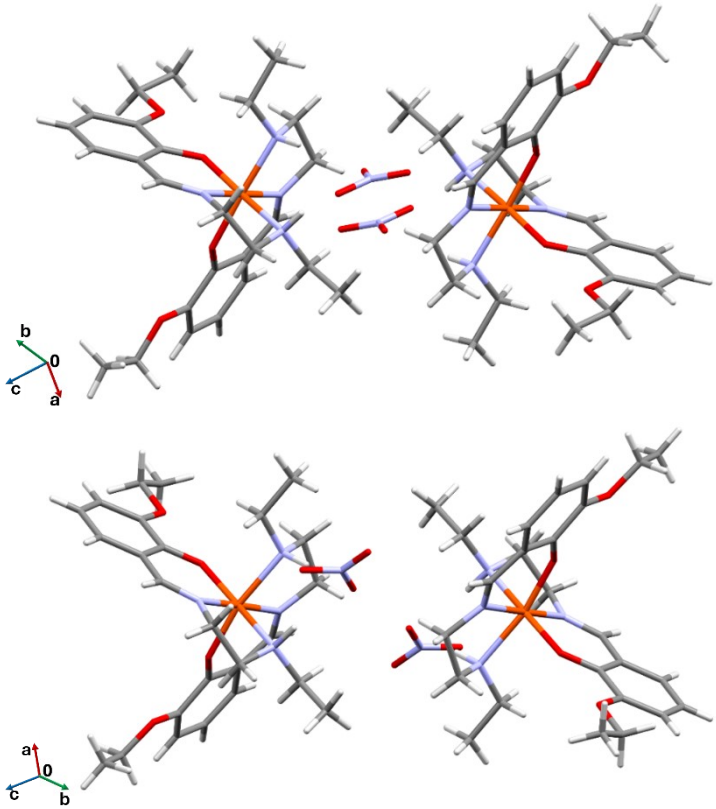

Supplementary Figure 6: Orientation of the NO_3^- anions in **1** at 150 (top) and 353 K (bottom).

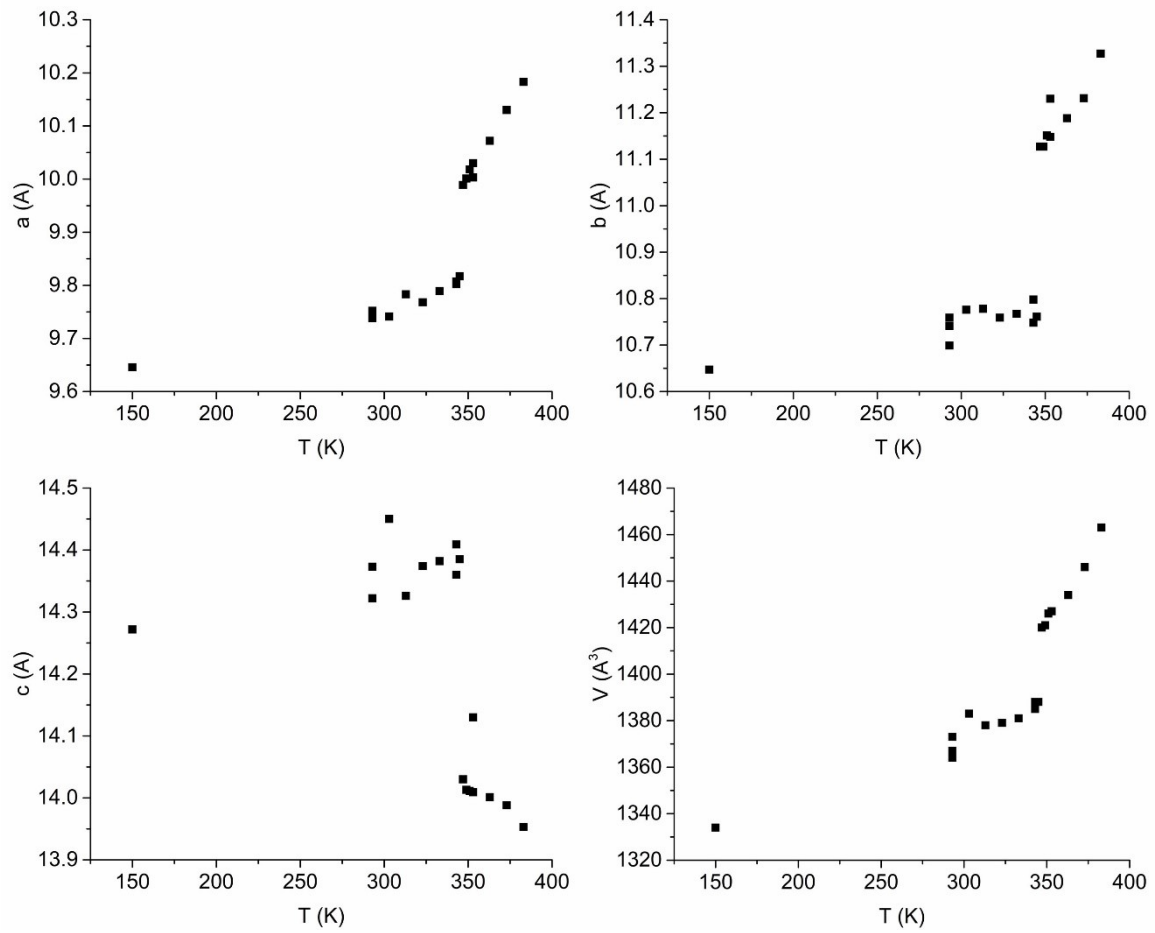

Supplementary Figure 7: Unit cell axis and volume variation as function of temperature in **1**.

2. Computational Details

Starting from the experimentally obtained LS and HS geometries from X-ray experiments, both the atomic coordinates and lattice parameters were optimized for each of the spin states, either having two (LS) or ten (HS) unpaired electrons per unit cell. Calculations were carried out within Density Functional Theory (DFT) using the Vienna Ab Initio Simulation Package (VASP) software,[82] employing periodic boundary conditions and using recommended Projector Augmented Wave (PAW) pseudopotentials for core electron density,[83] with a 415 eV cutoff for the kinetic energy of the plane waves used to define the valence electron density. This energy cutoff allows for low variations in total energy, already shown in the literature to result in variations below 1 meV for basis set improvement for smaller systems.[84] Optimizations were carried out using Gaussian smearing[85] with an energy width of 0.2 eV, yet the final total energy values were extrapolated to zero smearing. The convergence criterion for the electronic Self-Consistent Field (SCF) was set to 10^{-6} eV, whereas the atomic convergence criterion was set to 10^{-5} eV. Considering the relatively large size of the unit cell, for the **k**-points, a

Monkhorst-Pack[86] scheme was used only with the **Γ** point and with no shift of the **k**-points mesh.[87]

To determine the most suitable exchange-correlation functional for the systems under study, several functionals were benchmarked, employing in all studied functionals the semi-empirical parametrization of Grimme D3.[88] In order to observe the trend along different rungs of the Jacob's Ladder,[89] functionals belonging to different rungs were studied: the Vosko-Wilk-Nusair (VWN)[90] functional within the Local Density Approximation (LDA) rung; the Perdew-Burke-Ernzerhof (PBE)[91] functional within the Generalized Gradient Approximation (GGA) rung; both the strongly constrained and appropriately normed (SCAN)[92] and Tao-Perdew-Staroverov-Scuseria (TPSS)[93] functionals for the meta-GGAlevel; and finally, the Perdew-Burke-Ernzerhof functional with 25% of Hartree-Fock exchange (PBE0)[94] as an hybrid functional. The calculated HS and LS energy differences (E_{HS-LS}) were compared to the experimental enthalpy obtained through Differential Scan Calorimetry (DSC) to assess the most suited functional, for which metal-ligand distances and lattice parameters were compared with experimental values.

For the analysis and comparison of Hirshfeld surfaces and intermolecular interactions, the Crystal Explorer 21 software[95] was employed.

3. Calibration studies

Considering the experimental enthalpy of the LS-HS energy difference obtained with *DSC* of 11.6 kJ mol^{-1}, and that $H = U + PV$,[96] the total energy obtained using DFT can be directly compared with the experimental enthalpy, given that the calculations are made at 0 K, where the pressure effect is negligible. From the calibration of the functionals, TPSS was the one that reproduced better the LS-HS difference, with an E_{HS-LS} of 11.12 kJ mol^{-1}. For the rest of the functionals, the divergences were quite larger, see Supplementary Table 2. For the selected TPSS functional, metal-ligand distances were also compared with the experimental ones for the low spin and high spin configurations in Supplementary Table 3.

Supplementary Table 2: Spin transition energies (in kJ·mol^{-1}) obtained from the optimized coordinates and lattice parameters.

Functionals	E_{HS-LS}
VWN	546.76
PBE	231.10
SCAN	104.20
TPSS	11.12
PBE0	-57.01

Supplementary Table 3: Metal-Ligand distances for experimental and theoretical (TPSS) low-spin and high-spin configurations.

	Distance M-L (Å)					
	Fe-O(1)	**Fe-O(2)**	**Fe-N(1)**	**Fe-N(2)**	**Fe-N(3)**	**Fe-N(4)**
Exp. LS	1.877	1.887	2.029	1.918	1.922	2.058
TPSS LS	1.882	1.902	2.011	1.896	1.897	2.051
Exp. HS	1.902	1.904	2.022	2.038	2.160	2.146
TPSS HS	1.938	1.952	2.100	2.125	2.224	2.200

For the low-spin configuration, the experimental distances are in concordance, with the biggest deviation having only 1.15 % difference. As for the high-spin configuration, although the experimental values are close, they differ more (deviations up to 4.27 %) with a constant overestimation of the distances using TPSS. Considering that the high-spin experimental geometry is not 100% pure and had some mix with the low-spin structure, this difference may be a consequence of it.

Apart from the metal-ligand distances, the lattice parameters of both configurations were also compared, in order to ensure reliability of the chosen functional (*cf.* Supplementary Table 4).

Supplementary Table 4: Experimental and theoretical (TPSS) unit cell lattice parameters for the low-spin and high-spin configurations.

	Lattice vectors (Å)			Lattice Angles (º)			Volume (Å^3)
	a	***b***	***c***	**α**	**β**	**γ**	
Exp. LS	9.659	10.660	14.277	100.1	105.1	103.1	1338.255
TPSS LS	9.407	10.431	13.930	100.5	106.0	102.7	1237.895
Exp. HS	10.029	11.178	13.990	93.4	105.6	107.0	1427.326
TPSS HS	9.718	10.844	13.570	93.0	106.1	107.0	1299.272

Once again, the TPSS functional seems to simulate well the lattice parameters.

4. Hirshfeld Surfaces- Different Perspectives

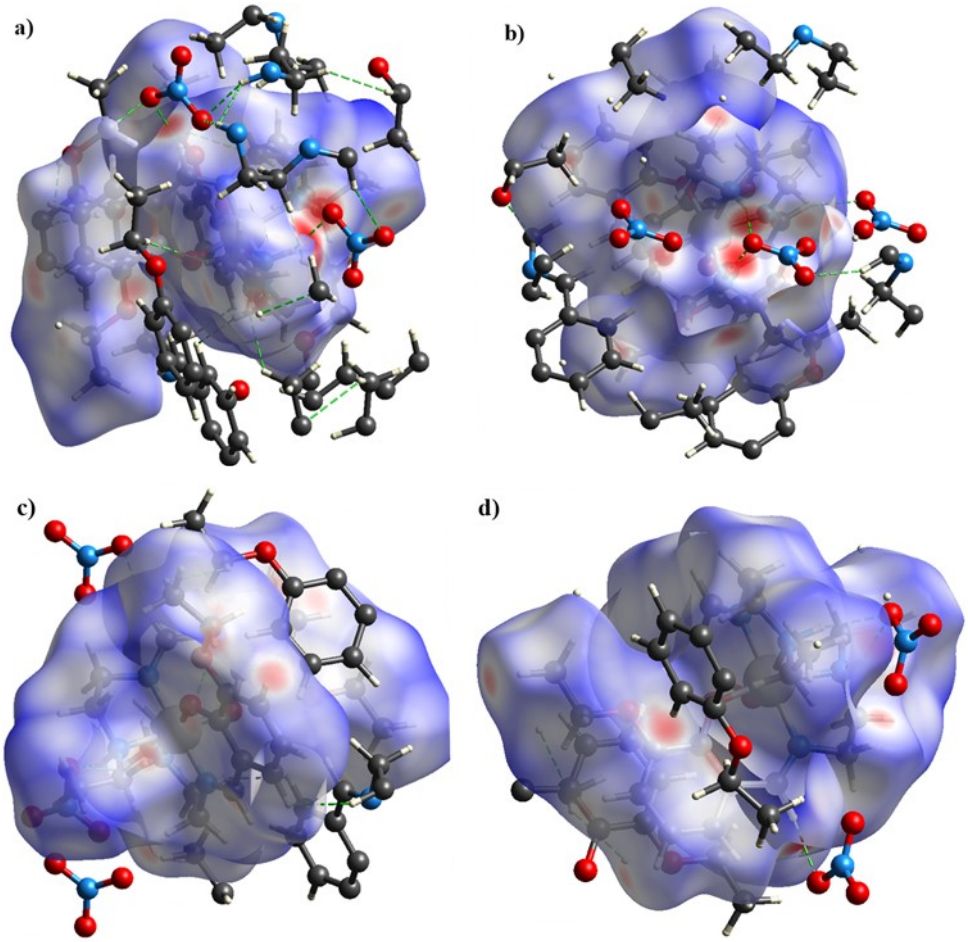

Supplementary Figure 8: Hirshfeld surface of low-spin (a, c) and high-spin (b, d) configurations, excluding the NO_3^- counterion, using TPSS functional for geometry optimization. The closer intermolecular interactions (up to 2.2 Å) are indicated in green dashed lines and evidenced by a red colour in the Hirshfeld surface, which correspond to O···H-C, O···H-N, and H···H interactions.

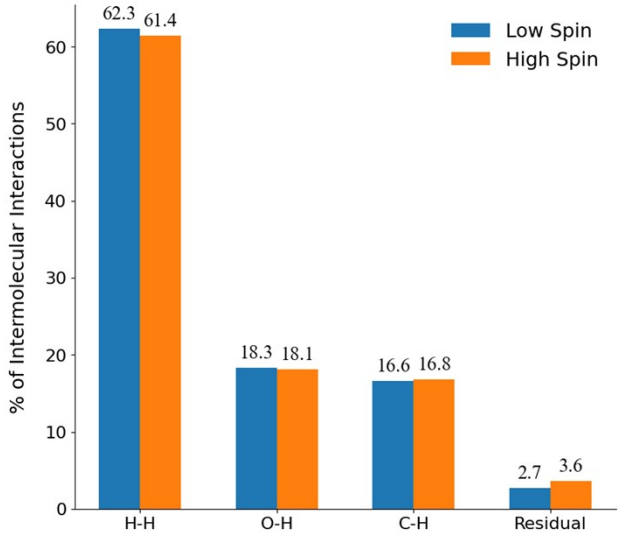

Supplementary Figure 9: Intermolecular interactions for the low-spin and high-spin configurations (in residual are included C···C, N···H, C···O), using the selected TPSS functional for geometry optimization.

5. Fingerprint Plots

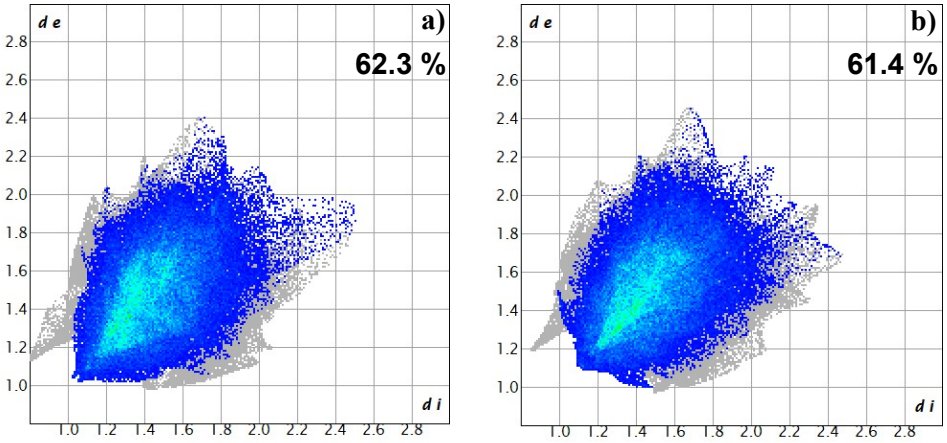

Supplementary Figure 10: Fingerprint plots of H-H interactions for the LS (a) and HS (b) configurations.

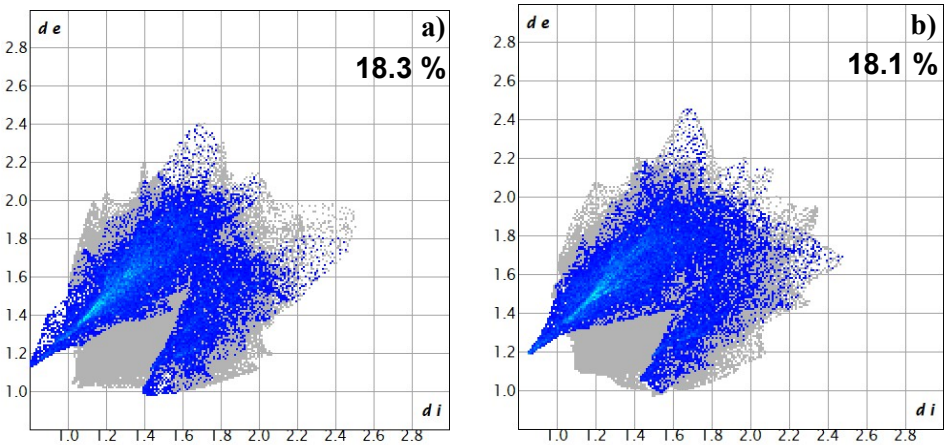

Supplementary Figure 11: Fingerprint plots of O-H interactions for the LS (a) and HS (b) configurations.

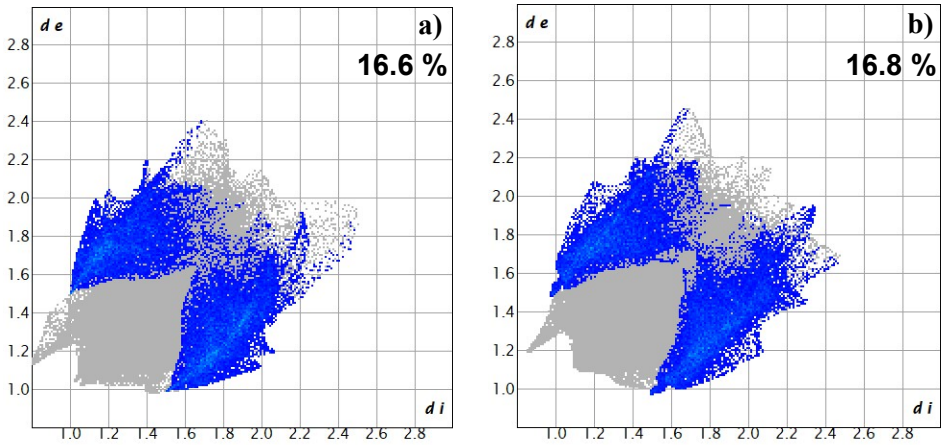

Supplementary Figure 12: Fingerprint plots of C-H interactions for the LS (a) and HS (b) configurations.

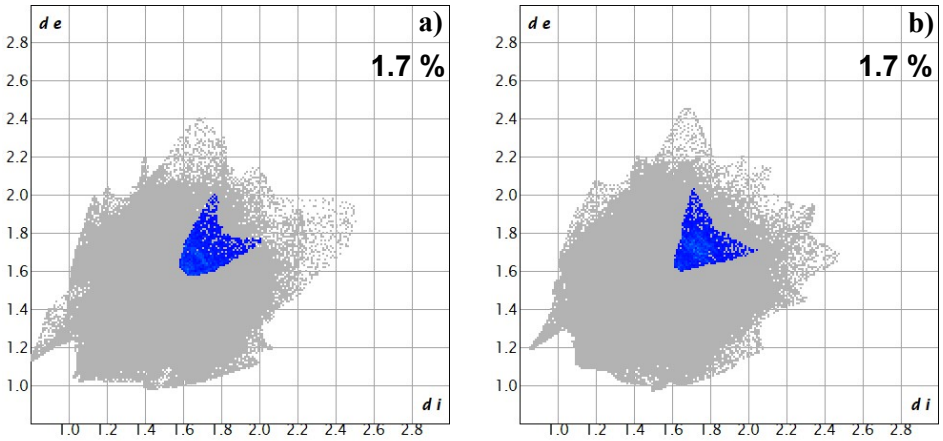

Supplementary Figure 13: Fingerprint plots of C-C interactions for the LS (a) and HS (b) configurations.

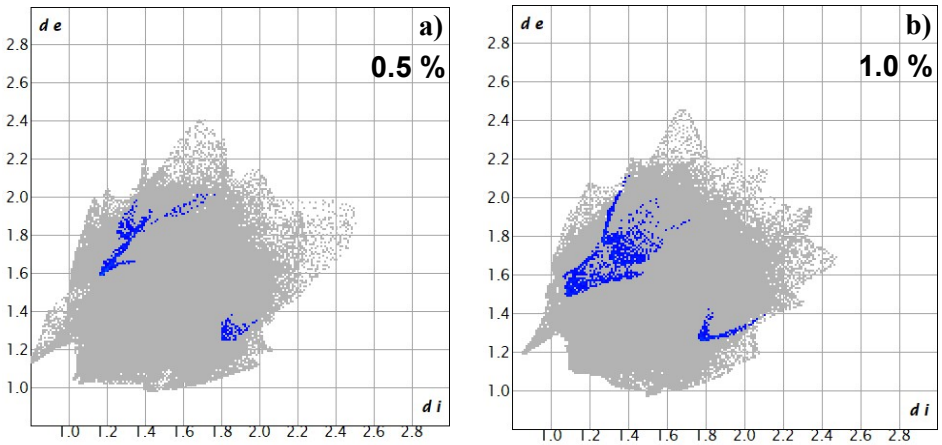

Supplementary Figure 14: Fingerprint plots of N-H interactions for the LS (a) and HS (b) configurations.

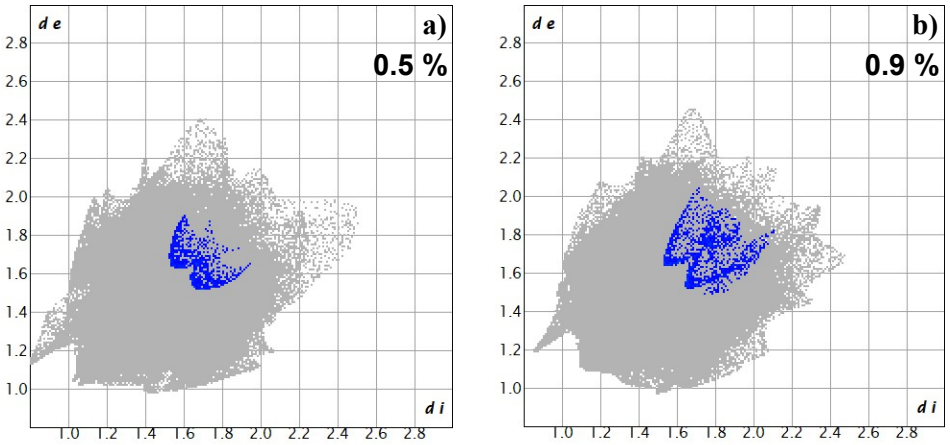

Supplementary Figure 15: Fingerprint plots of C-O interactions for the LS (a) and HS (b) configurations.

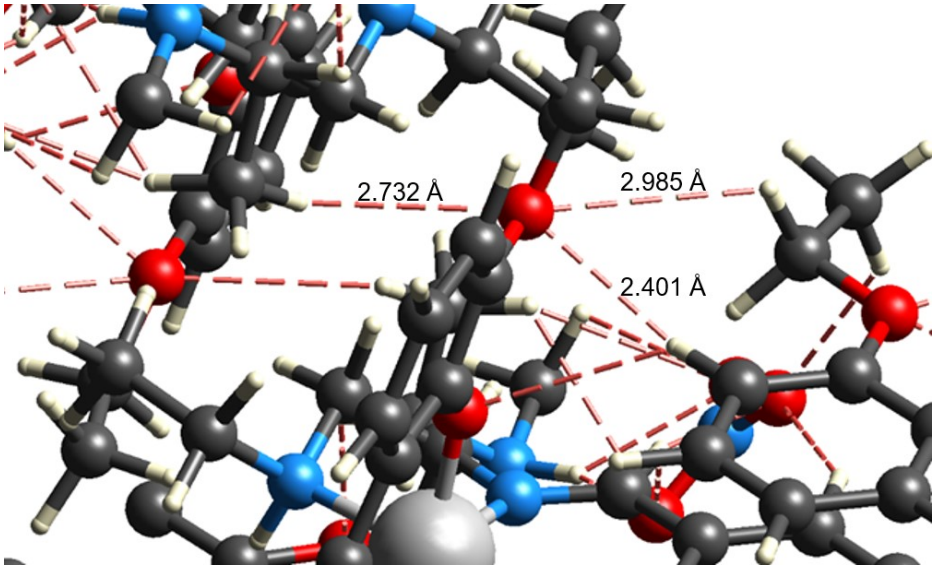

Supplementary Figure 16: Oxygen-hydrogen interactions involving the oxygen atom from EtO group, for the low-spin configuration. Fe, C, O, N, and H atoms are shown as light grey, dark grey red, blue, and white spheres, respectively, with shared colored bars denoting bonds between them, while O···H interactions are shown as red dashed lines.

Optical Microscopy Studies

Cryogenic optical microscopy measurements were carried out under a primary vacuum (in at a pressure of 10^{-6} mbar) on single crystals (length × width = 581 μm × 122 μm) using a Nikon Eclipse LV100 microscope (objective × 20, numerical aperture 0.45), equipped with a closed cycle Oxford Instruments nitrogen-flow cryostat and connected to a digital camera Allied Vision 1800 U-240C COLOR C-MOUNT, capable of capturing up to 126 frames per second. The OM images can be recorded in transmission (resp. reflection) geometry using backward (resp. upward) illumination by a tungsten halogen lamp, provided by the microscope. The sample was mounted in specific helium-tight cell designed for optical microscopy.[97] All measurements were performed in the range 330 K-360 K using a temperature scan rate of 0.25 K min^{-1}, which leads to an error of 0.1K on the measured temperature. The camera was configured to save ten images per second to record the spatiotemporal behavior of the spin transition. From every saved image, we can extract the optical density (OD), defined as (in case of transmission geometry):

$$OD = log_{10}\left(\frac{I_{incident}}{I_{transmitted}}\right), \quad (1)$$

where $I_{incident}$ corresponds to the bright field intensity while $I_{transmitted}$ corresponds to the intensity of the transmitted light through the single crystal. The OD which is the key parameter of the OM data analysis (recorded images) directly relates to the HS fraction, n_{HS}, of molecules undergoing the spin transition in the single crystal and therefore it should not be confused with the absolute HS fraction of molecules switching between the LS and HS states in the system. The HS fraction (n^*_{HS}) of metal ions in the HS state, among those switching between the two states, is then derived from OD data, through the relation:[98]

$$n^*_{HS} = \frac{< OD(x,y) > - < OD >_{LS}}{< OD >_{HS} - < OD >_{LS}}, \quad (2)$$

where $< OD >_{HS}$ and $< OD >_{LS}$ are respectively the spatially-averaged OD values in the HS and LS states and $< OD(x,y) > = \frac{\int OD(x,y)dxdy}{S}$ ($S =$ crystal surface) is the spatially averaged optical density over the crystal at given temperature, T. In addition, each image of the experimental OM data was split into three OD components: red, green, and blue, depending on the single crystal thickness and color. From one compound to another, the signal quality (signal to noise ratio), would perhaps be better, either in the red, green, or blue pixel. All the data are analyzed using Matlab programs specially developed for the analysis of OM data.

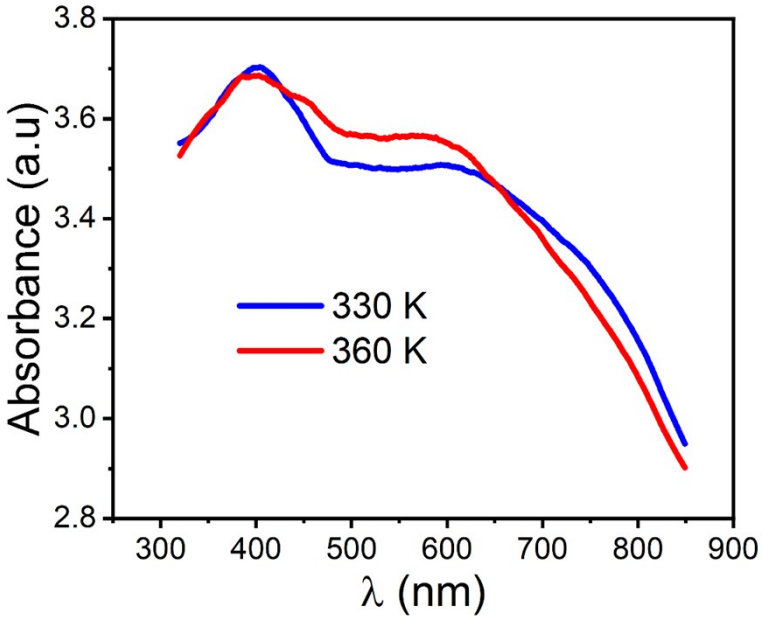

Supplementary Figure 17: Absorbance spectra of a pellet sample, made of ground Fe(3-EtO-salEen)$_2$]NO_3 crystals mixed with KBr in the wavelength range 320-850 nm, showing a broad absorption band covering a large part of the visible spectrum. The blue and red curves correspond to the responses of the LS (330 K) and the HS (360 K) states, respectively.

Linear and volumetric thermal expansion coefficients

The thermal expansion coefficients β_a, β_b and β_c, along the respective a, b and c lattice parameters are deduced from the data of Fig. S6, by plotting the thermal dependences of $\ln a$, $\ln b$ and $\ln c$. Using the simple formula $\beta_x = \frac{d}{dT} \ln x$ $(x = a, b, c)$, we could easily deduce all linear and volumetric thermal expansion coefficients in both LS and HS phases. The volumetric thermal expansion, β_V, is derived through the relation, $\beta_V = \frac{d}{dT} \ln V$. The estimated values of β_a, β_b, β_c and β_V are given in Supplementary Table 5.

Supplementary Table 5: Thermal expansion coefficient along a, b, c and Volume in the LS and HS states.

	Thermal expansion coefficients (K^{-1})			
	β_a	β_b	β_c	β_V
LS ($\times 10^{-5}$)	7.197	6.145	0.0160	20.01
HS	5.25	4.60	− 1.22	7.94

$(\times 10^{-4})$

These quantities could connected to the bulk modulus, B, through the simple relation, $B \simeq \frac{1}{\beta \frac{\Delta V}{\Delta S}}$, where the ratio $\frac{\Delta V}{\Delta S}$ is easily evaluated from the combination of XRD and calorimetric data. At least for the volumetric bulk modulus, one finds $B_{LS} \sim$ 20 GPa and $B_{HS} \sim$ 5 GPa.

	Bulk Moduls (GPa)			
	B_a	B_b	B_c	B_V
LS	55.6	65.1	-	20.0
HS	7.7	8.7	–	5.0

References

1. P. Gütlich, A. Hauser and H. Spiering, Thermal and Optical Switching of Iron(II) Complexes, *Angew. Chem., Int. Ed.*, 1994, **33**, 2024–2054.
2. P. Gütlich and H. A. Goodwin, Spin Crossover−An Overall Perspective, *Top. Curr. Chem.*, 2004, **233**, 1–47.
3. O. Sato, J. Tao and Y.-Z. Zhang, Control of Magnetic Properties through External Stimuli, *Angew. Chem., Int. Ed.*, 2007, **46**, 2152–2187.
4. O. Sato, J. Tao and Y.-Z. Zhang, Control of Magnetic Properties through External Stimuli (correction), *Angew. Chem., Int. Ed.*, 2007, **46**, 5049.
5. M. G. Reeves, E. Tailleur, P. A. Wood, M. Marchivie, G. Chastanet, P. Guionneau and S. Parsons, Mapping the cooperativity pathways in spin crossover complexes, *Chem. Sci.*, 2021, **12**, 1007–1015.
6. A. I. Nesterov, Y. S. Orlov, S. G. Ovchinnikov and S. V. Nikolaev, Cooperative phenomena in spin crossover systems, *Phys. Rev. B*, 2017, **96**, 134103.
7. N. Willenbacher and H. Spiering, The elastic interaction of high-spin and low-spin complex molecules in spin-crossover compounds, *J. Phys. C: Solid State Phys.*, 1988, **21**, 1423–1439.
8. H. Spiering and N. Willenbacher, Elastic interaction of high-spin and low-spin complex molecules in spin-crossover compounds. II, *J. Phys.: Condens. Matter*, 1989, **1**, 10089–10105.
9. K. Boukheddaden, I. Shteto, B. Hôo and F. Varret, Dynamical model for spin-crossover solids. II. Static and dynamic effects of light in the mean-field approach, *Phys. Rev. B*, 2000, **62**, 14806.
10. R. Bertoni, M. Lorenc, H. Cailleau, A. Tissot, J. Laisney, M. L. Boillot, L. Stoleriu, A. Stancu, C. Enachescu and E. Collet, Elastically driven cooperative response of a molecular material impacted by a laser pulse, *Nat. Mater.*, 2016, **15**, 606–610.
11. E. Milin, V. Patinec, S. Triki, E. E. Bendeif, S. Pillet, M. Marchivie, G. Chastanet and K. Boukheddaden, Elastic Frustration Triggering Photoinduced Hidden Hysteresis and Multistability in a Two-Dimensional Photoswitchable Hofmann-Like Spin-Crossover Metal-Organic Framework, *Inorg. Chem.*, 2016, **55**, 11652–11661.
12. P. Gütlich, A. B. Gaspar and Y. Garcia, Spin state switching in iron coordination compounds, *Beilstein J. Org. Chem.*, 2013, **9**, 342–391.
13. M. A. Halcrow, Spin-crossover compounds with wide thermal hysteresis, *Chem. Lett.*, 2014, **43**, 1178–1188.

14. G. Molnár, M. Mikolasek, K. Ridier, A. Fahs, W. Nicolazzi and A. Bousseksou, Molecular spin crossover materials: Review of the lattice dynamical properties, *Ann. Phys.*, 2019, **531**, 1900076.
15. T. K. Ekanayaka, K. P. Maity, B. Doudin and P. A. Dowben, Dynamics of spin crossover molecular complexes, *Nanomaterials*, 2022, **12**, 1742.
16. M. A. Halcrow, Structure: function relationships in molecular spin-crossover complexes, *Chem. Soc. Rev.*, 2011, **40**, 4119–4142.
17. J. J. Whittaker, P. Harding, P. J. K. Clegg and D. J. Harding, Structural origin of magnetic hysteresis in an iron(III) spin-crossover material, *Cryst. Growth Des.*, 2020, **20**, 7006–7011.
18. N. G. Spitsyna, M. A. Blagov, V. A. Lazarenko, R. D. Svetogorov, Y. V. Zubavichus, L. V. Zorina, O. Maximova, S. A. Yaroslavtsev, V. S. Rusakov, G. V. Raganyan, E. B. Yagubskii and A. N. Vasiliev, Peculiar spin-crossover behaviour in the 2D polymer $K[Fe^{III}(5Cl\text{-}thsa)_2]$, *Inorg. Chem.*, 2021, **60**, 17462–17479.
19. S. K. Karuppannan, A. Martin-Rodriguez, E. Ruiz, P. Harding, D. J. Harding, X. Yu, A. Tadich, B. Cowie, D. Qi and C. A. Nijhuis, Room temperature conductance switching in a molecular iron(III) spin-crossover junction, *Chem. Sci.*, 2021, **12**, 2381–2388.
20. R. Díaz-Torres, W. Phonsri, K. S. Murray, P. Harding and D. J. Harding, Supramolecular control of spin crossover in iron(III) complexes: parallel versus angled chains, *Cryst. Growth Des.*, 2022, **22**, 1543–1547.
21. K. J. Howard-Smith, A. R. Craze, R. Tokunaga, T. Taira, H. Min, M. J. Wallis, D. J. Fanna, S. Hayami and F. Li, High-temperature spin crossover in Fe^{III} N_4O_2 complexes incorporating an [R-sal_2-323] backbone, *Cryst. Growth Des.*, 2023, **23**, 1219–1228.
22. B. J. C. Vieira, L. C. J. Pereira, V. da Gama and J. C. Warenborgh, Structural features that modulate the sharpness of the spin crossover transition in $[Fe^{III}(5\text{-}X\text{-}qsal)_2]^+$-based salts, *CrystEngComm*, 2023, **25**, 6472–6477.
23. R. Díaz-Torres, G. Chastanet, E. Collet, E. Trzop, P. Harding and D. J. Harding, Bidirectional photoswitchability in an iron(III) spin crossover complex: symmetry-breaking and solvent effects, *Chem. Sci.*, 2023, **14**, 7185–7191.
24. A. Kacperkiewicz, R. J. Ortiz, S.-T. Chiu, P.-H. Lin and D. E. Herbert, Towards spin-crossover in pseudo-octahedral iron(III) complexes of strongly absorbing phenanthridine-based N^N^O^- ligands, *Inorg. Chim. Acta*, 2024, **563**, 121895.
25. A. Dürrmann, G. Hörner, D. Baabe, F. W. Heinemann, M. A. C. de Melo and B. Weber, Cooperative spin crossover leading to bistable and multi-inert system states in an iron(III) complex, *Nat. Commun.*, 2024, **15**, 7321.
26. B. Dey, J. Cirera, S. L. P. Ferreira, P. N. Martinho and V. Chandrasekhar, Peripheral ligand modification to tune spin crossover behaviour of Fe(III) complexes, *Cryst. Growth Des.*, 2025, **25**, 3065–3074.
27. R. Traiche, M. Sy, H. Oubouchou, G. Bouchez, F. Varret and K. Boukheddaden, Spatiotemporal observation and modeling of remarkable temperature scan rate effects on the thermal hysteresis in a spin-crossover single crystal, *J. Phys. Chem. C*, 2017, **121**, 11700–11708.
28. A. Cannizzo, L. Bellino, G. Florio, G. Puglisi and S. Giordano, Thermal control of nucleation and propagation transition stresses in discrete lattices with non-local interactions and non-convex energy, *Eur. Phys. J. Plus*, 2022, **137**, 569.
29. N. di Scala, N. E. I. Belmouri, M. A. P. Espejo and K. Boukheddaden, Three-dimensional electroelastic modeling of the nucleation and propagation of the spin domains in spin-crossover materials, *Phys. Rev. B*, 2022, **106**, 014422.

30. A. Slimani, F. Varret, K. Boukheddaden, D. Garrot, H. Oubouchou and S. Kaizaki, Velocity of the High-Spin Low-Spin Interface Inside the Thermal Hysteresis Loop of a Spin-Crossover Crystal, via Photothermal Control of the Interface Motion, *Phys. Rev. Lett.*, 2013, **110**, 087208.
31. M. Sy, F. Varret, K. Boukheddaden, G. Bouchez, J. Marrot, S. Kawata and S. Kaizaki, Structure-Driven Orientation of the High-Spin–Low-Spin Interface in a Spin-Crossover Single Crystal, *Angew. Chem., Int. Ed.*, 2014, **53**, 7539–7542.
32. E. M. Hernández, S. Zheng, H. J. Shepherd, D. S. Yufit, K. Ridier, S. Bedoui, W. Nicolazzi, V. Velázquez, S. Bonnet, G. Molnár and A. Bousseksou, Spatially Resolved Investigation and Control of the Bistability in Single Crystals of the [Fe(bbpya) $(NCS)_2$] Spin Crossover Complex, *J. Phys. Chem. C*, 2016, **120**, 27608–27617.
33. K. Ridier, S. Rat, H. J. Shepherd, L. Salmon, W. Nicolazzi, G. Molnár and A. Bousseksou, Spatiotemporal dynamics of the spin transition in $[Fe(HB(tz)_3)_2]$ single crystals, *Phys. Rev. B*, 2017, **96**, 134106.
34. H. Fourati, M. Ndiaye, M. Sy, S. Triki, G. Chastanet, S. Pillet and K. Boukheddaden, Light-induced thermal hysteresis and high-spin low-spin domain formation evidenced by optical microscopy in a spin-crossover single crystal, *Phys. Rev. B*, 2022, **105**, 174436.
35. K. Ridier, G. Molnár, L. Salmon, W. Nicolazzi and A. Bousseksou, Hysteresis, nucleation and growth phenomena in spin-crossover solids, *Solid State Sci.*, 2017, **74**, A1–A22.
36. R. Traiche, M. Sy and K. Boukheddaden, Elastic frustration in 1D spin-crossover chains: Evidence of multi-step transitions and self-organizations of the spin states, *J. Phys. Chem. C*, 2018, **122**, 4083–4096.
37. H. Oubouchou, Y. Singh and K. Boukheddaden, Magnetoelastic modeling of core-shell spin-crossover nanocomposites, *Phys. Rev. B*, 2018, **98**, 014106.
38. K. Affes, Y. Singh and K. Boukheddaden, Electro-Elastic Modeling of Thermal Spin Transition in Diluted Spin-Crossover Single Crystals, *Int. J. Mol. Sci.*, 2022, **23**, 13854.
39. N. di Scala, N. E. I. Belmouri, M. A. P. Espejo and K. Boukheddaden, Explaining the origin of the orientation of the front transformation in spin-transition crystals, *Phys. Rev. B*, 2022, **106**, 144107.
40. N. E. I. Belmouri, N. di Scala and K. Boukheddaden, 3D self-organization of spin crossover multi-layers emerging from the alliance of elastic anisotropy and lattice frustration, *J. Phys. Chem. Solids*, 2024, **190**, 111985.
41. B. Dey, J. Cirera, S. Mehta, L. P. Ferreira, R. Arumugam, A. Mondal, P. N. Martinho and V. Chandrasekhar, Steric Effects on Spin States in a Series of Fe(III) Complexes, *Cryst. Growth Des.*, 2023, **23**, 6668–6678.
42. M. A. Bento, T. Gomes, F. F. Martins, A. Gil, L. P. Ferreira, S. Barroso, C. S. B. Gomes, Y. Garcia and P. N. Martinho, The role of intermolecular interactions in $[Fe(X\text{-}salEen)_2]ClO_4$ spin crossover complexes, *Dalton Trans.*, 2024, **53**, 8791–8802.
43. R. T. Marques, L. P. Ferreira, C. S. B. Gomes, C. S. D. Lopes, C. E. S. Bernardes, N. K. Sarangi, T. E. Keyes and P. N. Martinho, Reversible single-crystal-to-single-crystal transformations in a saleen Fe(III) spin crossover sponge, *Cryst. Growth Des.*, 2023, **23**, 3222–3229.
44. A. I. Vicente, A. Joseph, L. P. Ferreira, M. de Deus Carvalho, V. H. N. Rodrigues, M. Duttine, H. P. Diogo, M. E. Minas da Piedade, M. J. Calhorda and P. N. Martinho, Dynamic spin interchange in a tridentate Fe(III) Schiff-base compound, *Chem. Sci.*, 2016, **7**, 4251–4258.
45. T. Boonprab, S. J. Lee, S. G. Telfer, K. S. Murray, W. Phonsri, G. Chastanet, E. Collet, E. Trzop, G. N. L. Jameson, P. Harding and D. J. Harding, The First Observation of Hidden Hysteresis in an Iron(III) Spin-Crossover Complex, *Angew. Chem., Int. Ed.*, 2019, **58**, 11811–11815.
46. R. Bertoni, E. Collet, H. Cailleau, M.-L. Boillot, A. Tissot, J. Laisney, C. Enachescu and M. Lorenc, Temperature dependence of the cooperative out-of-equilibrium elastic switching in a spin-crossover material, *Phys. Chem. Chem. Phys.*, 2019, **21**, 6606–6612.

47. W. Phonsri, L. C. Darveniza, S. R. Batten and K. S. Murray, Heteroleptic and Homoleptic Iron(III) Spin-Crossover Complexes; Effects of Ligand Substituents and Intermolecular Interactions between Co-Cation/Anion and the Complex, *Inorganics*, 2017, **5**, 51.
48. V. Russell, M. Scudder and I. Dance, The crystal supramolecularity of metal phenanthroline complexes, *J. Chem. Soc., Dalton Trans.*, 2001, 789–799.
49. A. Gil, M. Sodupe and J. Bertran, Unusual hydrogen bonds in $[AH_3–H_3O]^{+\cdot}$ radical cations (A = C, Si, Ge, Sn and Pb): Single-electron hydrogen bond, proton-hydride hydrogen bond and formation of $[H_2AOH_2]^{+\cdot}–H_2$ complexes, *Chem. Phys. Lett.*, 2004, **395**, 27–32.
50. A. Gil, A. Sanchez-Gonzalez and V. Branchadell, Unraveling the Modulation of the Activity in Drugs Based on Methylated Phenanthroline When Intercalating between DNA Base Pairs, *J. Chem. Inf. Model.*, 2019, **59**, 3989–3995.
51. S. Elleuchi, I. O. de Luzuriaga, A. Sanchez-Gonzalez, X. Lopez, K. Jarraya, M. J. Calhorda and A. Gil, Computational studies on the binding preferences of molybdenum(II) phenanthroline complexes with duplex DNA. The important role of the ancillary ligands, *Inorg. Chem.*, 2020, **59**, 12711–12721.
52. Á. Sánchez-González and A. Gil, Elucidating the intercalation of methylated 1,10-phenanthroline with DNA: the important weight of the CH/H interactions and the selectivity of CH/π and CH/n interactions, *RSC Adv.*, 2021, **11**, 1553–1563.
53. Á. Sánchez-González, T. G. Castro, M. Melle-Franco and A. Gil, From groove binding to intercalation: unravelling the weak interactions and other factors modulating the modes of interaction between methylated phenanthroline-based drugs and duplex DNA, *Phys. Chem. Chem. Phys.*, 2021, **23**, 26680–26695.
54. C. Chong, H. Mishra, K. Boukheddaden, S. Denise, G. Bouchez, E. Collet, J.-C. Ameline, A. D. Naik, Y. Garcia and F. Varret, Electronic and Structural Aspects of Spin Transitions Observed by Optical Microscopy. The Case of $[Fe(ptz)_6](BF_4)_2$, *J. Phys. Chem. B*, 2010, **114**, 1975–1984.
55. F. Varret, A. Slimani, K. Boukheddaden, C. Chong, H. Mishra, E. Collet, J. Haasnoot and S. Pillet, The propagation of the thermal spin transition of $[Fe(btr)_2(NCS)_2]\cdot H_2O$ single crystals, observed by optical microscopy**,** *New J. Chem.*, 2011, **35**, 2333–2340.
56. A. Slimani, F. Varret, K. Boukheddaden, C. Chong, H. Mishra, J. Haasnoot and S. Pillet, Visualization and quantitative analysis of spatiotemporal behavior in a first-order thermal spin transition: A stress-driven multiscale process, *Phys. Rev. B*, 2011, **84**, 094442.
57. C. Chong, A. Slimani, F. Varret, K. Boukheddaden, E. Collet, J.-C. Ameline, R. Bronisz and A. Hauser, The kinetics features of a thermal spin transition characterized by optical microscopy on the example of $[Fe(bbtr)_3](ClO_4)_2$ single crystals: Size effect and mechanical instability, *Chem. Phys. Lett.*, 2011, **504**, 29–33.
58. N. E. I. Belmouri, G. Bouchez, J. A. Real, F. J. Valverde-Muñoz and K. Boukheddaden, Spatiotemporal imaging of a synergistic light control of the nucleation mechanism in a Hofmann-type spin-transition single crystal, *Appl. Mater. Today*, 2025, **44**, 102748.
59. K. Boukheddaden and M. Sy, Direct optical microscopy observation of photo-induced effects and thermal relaxation in a spin crossover single crystal, Curr. *Inorg. Chem.*, 2016, **6**, 40–48.
60. K. Boukheddaden, H. Fourati, Y. Singh and G. Chastanet, Evidence of Photo-Thermal Effects on the First-Order Thermo-Induced Spin Transition of $[\{Fe(NCSe)(py)_2\}_2$(m-bpypz)] Spin-Crossover Material, *Magnetochemistry*, 2019, **5**, 21.
61. H. Fourati and K. Boukheddaden, Experimental evidence for the elastic long-range character of the spin crossover transition in cooperative single crystals, *Phys. Rev. B*, 2020, **101**, 224101.
62. A.-I. Popa, L. Stoleriu and C. Enachescu; Tutorial on the elastic theory of spin crossover materials, *J. Appl. Phys.,* 2021, **129**, 131101.

63. C. Enachescu and W. Nicolazzi. Elastic models, lattice dynamics and finite size effects in molecular spin crossover systems, *Comptes Rendus. Chimie*, 2018, **21**, pp. 1179-1195.
64. K. Nakamura, W. Ota, M. Alashoor, G. Li, S. R. Maity, Y. Nakamura, O. Stefanczyk, K. Nakabayashi, E. Collet, S.-i. Ohkoshi and L. Guérin, Pathway from Molecular Strain to Crystal Domains and Cracks in Layered Co–W Charge-Transfer Materials. *Chem. Mater.*, 2025, **37**, 6004-6014.
65. A. Slimani, K. Boukheddaden and K. Yamashita, Effect of intermolecular interactions on the nucleation, growth, and propagation of like-spin domains in spin-crossover materials, *Phys Rev. B*, 2015, **92**, 014111
66. H. Fourati, E. Milin, A. Slimani, G. Chastanet, Y. Abid, S. Triki and K. Boukheddaden, Interplay between a crystal's shape and spatiotemporal dynamics in a spin transition material, *Phys. Chem. Chem. Phys.*, 2018, **20**, 10142–10154.
67. M. Sy, R. Traiche, H. Fourati, Y. Singh, F. Varret and K. Boukheddaden, Spatiotemporal investigations on light-driven high-spin–low-spin interface dynamics in the thermal hysteresis region of a spin-crossover single crystal, *J. Phys. Chem. C*, 2018, **122**, 20952–20962.
68. I. Nemec, R. Herchel and Z. Trávníček, The relationship between the strength of hydrogen bonding and spin crossover behaviour in a series of iron(III) Schiff base complexes, *Dalton Trans.*, 2015, **44**, 4474–4484.
69. W. Phonsri, P. Harding, L. Liu, S. G. Telfer, K. S. Murray, B. Moubaraki, T. M. Ross, G. N. L. Jameson and D. J. Harding. Solvent modified spin crossover in an iron(III) complex: phase changes and an exceptionally wide hysteresis. *Chem. Sci.*, 2017, **8**, 3949-3959.
70. P. J. van Koningsbruggen, Y. Maeda, H. Oshio, Iron(III) Spin Crossover Compounds, *Top. Curr. Chem.*, 2004, **233**, 259–324.
71. I. S. Jahro, D. Onggo, Ismunandar, S. I. Rahayu, M. C. Muñoz, A. B. Gaspar, M. Seredyuk, P. Gütlich and J. A. Real. Synthesis, crystal structure and magnetic properties of the spin crossover system $[Fe(pq)_3]^{2+}$, *Inorg. Chim. Acta*, 2008, **361**, 4047-4054.
72. G. M. Sheldrick, A Short History of SHELX, *Acta Crystallogr., Sect. A: Found. Crystallogr.*, 2008, **64**, 112.
73. F. J. Valverde-Muñoz, R. Kazan, K. Boukheddaden, M. Ohba, J. A. Real and T. Delgado, Downsizing of Nanocrystals While Retaining Bistable Spin Crossover Properties in Three-Dimensional Hofmann-Type $\{Fe(pz)[Pt(CN)_4]\}$–Iodine Adducts, *Inorg. Chem.*, 2021, **60**, 8851–8860.
74. R. Li, G. Levchenko, F. J. Valverde-Muñoz, A. B. Gaspar, V. V. Ivashko, Q. Li, B. Liu, M. Yuan, H. Fylymonov and J. A. Real, Pressure Tunable Electronic Bistability in Fe(II) Hofmann-like Two-Dimensional Coordination Polymer $[Fe(Fpz)_2Pt(CN)_4]$: A Comprehensive Experimental and Theoretical Study, *Inorg. Chem.*, 2021, **60**, 16016–16028.
75. K. Boukheddaden, M. H. Ritti, G. Bouchez, M. Sy, M. M. Dîrtu, M. Parlier, J. Linares and Y. Garcia, Quantitative contact pressure sensor based on spin crossover mechanism for civil security applications, *J. Phys. Chem. C*, 2018, **122**, 7597–7604.
76. M. Mikolasek, M. D. Manrique-Juarez, H. J. Shepherd, K. Ridier, S. Rat, V. Shalabaeva, A.-C. Bas, I. E. Collings, F. Mathieu, J. Cacheux, T. Leichle, L. Nicu, W. Nicolazzi, L. Salmon, G. Molnár and A. Bousseksou, Complete set of elastic moduli of a spin-crossover solid: Spin-state dependence and mechanical actuation, *J. Am. Chem. Soc.*, 2018, **140**, 8970–8979.
77. V. Ksenofontov, H. Spiering, A. Schreiner, G. Levchenko, H. A. Goodwin and P. Gütlich, The influence of hydrostatic pressure on hysteresis phase transition in spin crossover compounds, *J. Phys. Chem. Solids*, 1999, **60**, 393–399.
78. B. Xu, Y. Li, B. Baptiste, L.-M. Chamoreau, D. Paliwoda, S. Mi, G. Molnár, K. Boukheddaden and R. Lescouëzec, Deciphering the Unusual Pressure-Induced Electron

Transfer in the Molecular Switch $\{[Fe(Tp)(CN)_3]_2[Co(vbik)_2]_2\}\cdot(BF_4)_2\cdot 2MeOH$, *Chem. Mater.*, 2024, **36**, 8990–9001.

79. A. Yangui, M. Sy, L. Li, Y. Abid, P. Naumov and K. Boukheddaden, Rapid and robust spatiotemporal dynamics of the first-order phase transition in crystals of the organic-inorganic perovskite $(C_{12}H_{25}NH_3)_2PbI_4$, *Scientific reports*, 2015, **5**, 16634.
80. J. Yoon, H. Kim, X. Chen, N. Tamura, B. S. Mun, C. Park and H. Ju, Controlling the temperature and speed of the phase transition of VO_2 microcrystals, *ACS App. Mater. Interfaces*, 2016, **8**, 2280-2286.
81. C. F. MacRae, I. Sovago, S. J. Cottrell, P. T. A. Galek, P. McCabe, E. Pidcock, M. Platings, G. P. Shields, J. S. Stevens, M. Towler and P. A. Wood, Mercury 4.0: From visualization to analysis, design and prediction, *J. Appl. Crystallogr.*, 2020, **53**, 226–235.
82. G. Kresse and J. Furthmüller, Efficient iterative schemes for ab initio total-energy calculations using a plane-wave basis set, *Phys. Rev. B*, 1996, **54**, 11169–11186.
83. J. Hafner, Ab-initio simulations of materials using VASP: Density-functional theory and beyond, *J. Comput. Chem.*, 2008, **29**, 2044–2078.
84. P. Janthon, S. M. Kozlov, F. Viñes, J. Limtrakul and F. Illas, Establishing the accuracy of broadly used density functionals in describing bulk properties of transition metals, *J. Chem. Theory Comput.*, 2013, **9**, 1631–1640.
85. M. Erdol, A. S. Konukman, A. S. Oktem, The effect of cell-size, cross-linking ratio, and force fields on the determination of properties of epoxy crosslinked by heuristic protocol, *Model. Simul. Mater. Sci. Eng.*, 2021, **29**, 085004.
86. H. J. Monkhorst and J. D. Pack, Special points for Brillouin-zone integrations, *Phys. Rev. B*, 1976, **13**, 5188–5192.
87. P. Kratzer and J. Neugebauer, The basics of electronic structure theory for periodic systems, *Front. Chem.*, 2019, **7**, 106.
88. S. Grimme, J. Antony, S. Ehrlich and H. Krieg, A consistent and accurate ab initio parametrization of density functional dispersion correction (DFT-D) for the 94 elements H-Pu, *J. Chem. Phys.*, 2010, **132**, 154104.
89. F. Tran, J. Stelzl and P. Blaha, Rungs 1 to 4 of DFT Jacob's ladder: Extensive test on the lattice constant, bulk modulus, and cohesive energy of solids, *J. Chem. Phys.*, 2016, **144**, 204120.
90. S. H. Vosko, L. Wilk and M. Nusair, Accurate spin-dependent electron liquid correlation energies for local spin density calculations: a critical analysis, *Can. J. Phys.*, 1980, **58**, 1200-1211.
91. J. P. Perdew, K. Burke and M. Ernzerhof, Generalized gradient approximation made simple, *Phys. Rev. Lett.*, 1996, **77**, 3865–3868.
92. J. Sun, A. Ruzsinszky and J. P. Perdew, Strongly constrained and appropriately normed semilocal density functional, *Phys. Rev. Lett.*, 2015, **115**, 036402.
93. J. Tao, J. P. Perdew, V. N. Staroverov and G. E. Scuseria, Climbing the density functional ladder: Nonempirical meta–generalized gradient approximation designed for molecules and solids, *Phys. Rev. Lett.*, 2003, **91**, 146401.
94. C. Adamo and V. Barone, Toward reliable density functional methods without adjustable parameters: The PBE0 model, *J. Chem. Phys.*, 1999, **110**, 6158–6170.
95. P. R. Spackman, M. J. Turner, J. J. McKinnon, S. K. Wolff, D. J. Grimwood, D. Jayatilaka and M. A. Spackman, CrystalExplorer: a program for Hirshfeld surface analysis, visualization and quantitative analysis of molecular crystals, *J. Appl. Crystallogr.*, 2021, **54**, 1006–1011.
96. L. A. Girifalco, Statistical Mechanics of Solids, Oxford University Press, Oxford, 2000.
97. M. Sy, PhD thesis, Université Paris-Saclay, 2016.
98. L. Sun, M. Ndiaye, N. Belmouri, K. Robeyns, A. Rotaru, K. Boukheddaden and Y. Garcia, Spin crossover coordination polymers with pyridine-like modification through selective guest molecules, *Cryst. Growth Des.*, 2022, **22**, 7555–7563.